Investigation of tone generation in ideally expanded supersonic planar impinging jets using large-eddy simulation

Romain Gojon[1,†], Christophe Bogey[1] and Olivier Marsden[1]

[1]Laboratoire de Mécanique des Fluides et d'Acoustique, UMR CNRS 5509, Ecole Centrale de Lyon, Université de Lyon, 69134 Ecully CEDEX, France

The generation of tones in a supersonic planar jet impinging on a flat plate normally has been investigated by performing compressible large-eddy simulations using low-dissipation and low-dispersion finite differences. At the exit of a straight nozzle of height h, the jet is ideally expanded, and has a Mach number of 1.28 and a Reynolds number of 5×10^4. Four distances between the nozzle and the plate between $3.94h$ and $9.1h$ have been considered. Flow snapshots and mean velocity fields are first presented. The variations of turbulence intensities and of the convection velocity in the jet shear layers are then examined. The properties of the jet near fields are subsequently described, in particular by applying Fourier decomposition to the pressure fields. Several coexisting tones appear to be generated by aeroacoustic feedback loops establishing between the nozzle lip and the flat plate, which also lead to the presence of hydrodynamic–acoustic standing waves. The tone frequencies are consistent with those given by the aeroacoustic feedback model and with measurements for high-aspect-ratio rectangular jets. The jet oscillation modes at these frequencies are characterized, and found to agree with experimental data. Their symmetric or antisymmetric natures are shown to be well predicted by a wave analysis carried out using a vortex sheet model of the jet, providing the allowable frequency ranges for the upstream-propagating acoustic waves. Thus, it is possible, for an ideally expanded impinging planar jet to predict both the frequencies of the tones and the symmetric or antisymmetric nature of the corresponding oscillation modes by combining the aeroacoustic feedback model and the wave analysis.

Key words: aeroacoustics, jet noise

1. Introduction

Jets impinging on a flat plate have been studied experimentally by many authors over the past sixty years. In some cases, very intense tones have been observed in the acoustic field. In his pioneering work, Powell (1953) suggested that they are due to a feedback mechanism between turbulent structures propagating downstream from the nozzle lip to the plate and acoustic waves propagating upstream from the plate to the nozzle lip. This self-sustaining oscillating flow for which a free shear layer

† Email address for correspondence: romain.gojon@ec-lyon.fr

impinges on a solid boundary is similar to the oscillating flow over a cavity (Rockwell & Naudascher 1978), which also generates tones.

Subsonic round jets at a Mach number between 0.3 up to 0.9 impinging on a flat plate normally have been studied notably by Ho & Nosseir (1981) and Nosseir & Ho (1982). Their near pressure fields were described using microphones, and a simplified model predicting the frequencies of the feedback mechanism occurring between the nozzle and the plate was proposed. Supersonic impinging round jets have also been investigated experimentally by Henderson & Powell (1993), Krothapalli *et al.* (1999) and Henderson, Bridges & Wernet (2005), and more recently by Risborg & Soria (2009), Buchmann *et al.* (2011) and Mitchell, Honnery & Soria (2012) using high-speed optical measurements. In some cases, a feedback mechanism similar to that encountered in subsonic jets was found. This mechanism is observed very often when the jets are ideally expanded, but less frequently and only for certain nozzle-to-plate distances when the jets are imperfectly expanded. Henderson *et al.* (2005) suggested that in the latter case, the feedback loop establishes only when a Mach disk forms upstream from the plate.

Subsonic impinging planar jets also produce intense tones. However, compared to round jets, the tones are generated for lower flow velocities, as noted by Arthurs & Ziada (2012). Supersonic impinging planar jets have been studied by Krothapalli (1985) by considering rectangular jets of moderate aspect ratio. In some cases, two tone frequencies, namely a screech tone frequency and an impinging tone frequency, emerge in the sound spectra. A staging behaviour was noted for the impinging tone frequency. Later, Norum (1991) and Tam & Norum (1992) also studied supersonic impinging planar jets. For certain jets, they obtained acoustic spectra with two emerging tone frequencies. The lower and the upper tone frequencies are respectively associated with breathing (symmetric oscillation) modes and with flapping (antisymmetric oscillation) modes of the jets. Similar tone frequencies have been found in a two-dimensional (2-D) simulation by Hourigan, Rudman & Brocher (1996). In order to explain the symmetric or antisymmetric nature of the jet oscillations, Tam & Norum (1992) suggested that the second part of the feedback loop is related to the upstream-propagating neutral acoustic wave modes of the vortex sheet model of the jets. This model provides an allowable frequency range for each of these modes. The two tones emerging in the experiments of Norum (1991) were then noted to fall into the ranges thus obtained for the first symmetric and the first antisymmetric modes, in agreement with the nature of the corresponding jet oscillation modes. Later, several tone frequencies were also measured by Thurow, Samimy & Lempert (2002) for supersonic rectangular impinging jets using a real-time flow visualization technique. A coupling between the organization of the hydrodynamic structures in the shear layers of the jets and the degree of resonance of the feedback mechanism was pointed out.

In the present work, four large-eddy simulations (LES) of an ideally expanded planar jet impinging on a flat plate normally are carried out on Cartesian meshes containing between 184 and 263 million points in order to investigate the tone generation in this flow configuration. The jet is characterized by a Mach number of 1.28 and a Reynolds number of 5×10^4, and nozzle-to-plate distances varying from $3.94h$ up to $9.1h$ are considered. The properties of the jet flow and acoustic fields are described, and compared with experimental data and with empirical and theoretical models. In particular, the effects of the nozzle-to-plate distance on the tone frequencies of the feedback loop and on the corresponding jet oscillation modes are examined.

The paper is organized as follows. The main parameters of the jets and of the simulations are presented in § 2. Aerodynamic results including flow snapshots, mean velocity fields, turbulence intensities and convection velocity are shown in § 3. The acoustic fields are analysed and compared with measurements in § 4. The properties of the tones produced by the aeroacoustic feedback mechanism establishing in the jets are discussed in § 5 by applying Fourier decomposition to the near pressure field. A new approach combining the aeroacoustic feedback model and a wave analysis using a vortex sheet jet model is developed. It aims to determine the most likely possible tone frequencies of the feedback mechanism and the antisymmetric or symmetric natures of the corresponding oscillation modes. Finally, concluding remarks are given in § 6.

2. Large-eddy simulations of supersonic planar jets

2.1. *Jet parameters*

Four large-eddy simulations of a jet impinging on a flat plate normally are performed. The jet originates from a planar straight nozzle of height h and width $l = 3.25h$ in the spanwise direction. The lip thickness is $e = 0.5h$ and periodic conditions are imposed in the spanwise direction. Nozzle-to-plate distances L equal to $3.94h$, $5.5h$, $8.27h$ and $9.1h$ are considered. The four cases are consequently referred to as JetL3.9, JetL5.5, JetL8.3 and JetL9.1. The ejection conditions of the jet and the nozzle-to-plate distances are similar to those in the experimental study of Thurow *et al.* (2002). Thus, the jet is ideally expanded, and has a Mach number of $\mathcal{M}_j = u_j/a_j = 1.28$, where u_j is the jet exit velocity and a_j is the speed of sound at the nozzle exit. The jet Reynolds number is $Re_h = u_j h/\nu = 5 \times 10^4$, where ν is the kinematic molecular viscosity. At the nozzle exit, a Blasius boundary-layer mean velocity profile of $0.075h$ wide is imposed. Finally, low-amplitude random vortical disturbances not correlated in the spanwise direction are added in the boundary layer in the nozzle $0.25h$ upstream from the exit in order to generate velocity fluctuations at the nozzle exit. The strength α of the forcing is similar to those used in Bogey, Marsden & Bailly (2011). It is set to 0.02, allowing us to reach peak turbulent intensities between 5 % and 10 % at the nozzle exit, as it will be reported in the next section.

2.2. *Numerical parameters*

The unsteady compressible Navier–Stokes equations are solved on a Cartesian mesh for which x, y and z denote the longitudinal, lateral and spanwise directions, respectively. An explicit six-stage Runge–Kutta algorithm is used for time integration, and low-dispersion eleven-point explicit centred finite differences are employed for spatial derivation (Bogey & Bailly 2004; Berland *et al.* 2007b). At the end of each time step, a sixth-order eleven-point filtering (Bogey, de Cacqueray & Bailly 2009) is applied to the flow variables in order to remove grid-to-grid oscillations and to relax turbulent energy from scales at wavenumbers close to the grid cutoff wavenumber. Thus, the filtering acts as a subgrid-scale model in the LES (Bogey & Bailly 2006, 2009; Fauconnier, Bogey & Dick 2013; Kremer & Bogey 2015). The radiation conditions of Tam & Dong (1994) are implemented at the upstream and lateral boundaries of the computational domain. A sponge zone combining grid stretching and Laplacian filtering is also used to damp the turbulent fluctuations before they reach the lateral boundaries. This numerical set up has been used in past studies to simulate round subsonic jets at $\mathcal{M}_j = 0.9$ (Bogey *et al.* 2011; Bogey, Marsden & Bailly 2012; Bogey & Marsden 2016) and an underexpanded planar jet at a fully
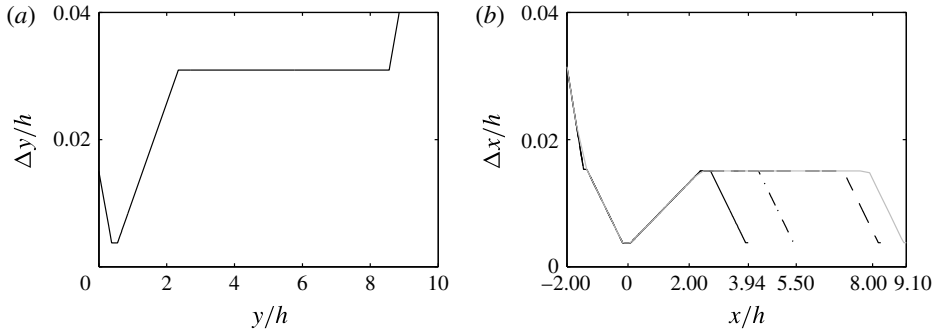
FIGURE 1. Representation of (*a*) the lateral mesh spacings and (*b*) the axial mesh spacings: —— JetL3.9, — · — JetL5.5, – – – JetL8.3 and —— JetL9.1.

	L	n_x	n_y	n_z	Number of points
JetL3.9	$3.94h$	799	1051	219	184×10^6
JetL5.5	$5.5h$	903	1051	219	208×10^6
JetL8.3	$8.27h$	1087	1051	219	250×10^6
JetL9.1	$9.1h$	1142	1051	219	263×10^6

TABLE 1. Parameters of the grids.

expanded Mach number of $\mathcal{M}_j = 1.55$ (Berland, Bogey & Bailly 2007*a*) for instance. In the present LES, adiabatic conditions are imposed at the nozzle walls and the flat plate. A shock-capturing filtering is applied in order to avoid Gibbs oscillations near shocks. It consists of applying a conservative second-order filter at a magnitude determined each time step using a shock sensor (Bogey *et al.* 2009). This method was successfully used by de Cacqueray, Bogey & Bailly (2011) for the LES of an overexpanded jet at $\mathcal{M}_j = 3.3$.

The simulations are carried out using an OpenMP-based in-house solver, and a total of 200 000 iterations are computed in each case after the transient period. The temporal discretization is equal to $\Delta t = 0.0025h/u_j$, yielding a simulation time of $500h/u_j$. The parameters of the Cartesian grids used in the four LES are reported in table 1. The grids contain between 184 and 263 million points. The variations of the axial and lateral mesh spacings are represented in figure 1. The minimal axial mesh spacing, near the nozzle lip and the flat plate, is set to $\Delta x = 0.00375h$, and the maximal axial mesh spacing is $\Delta x = 0.015h$. The lateral mesh spacings are equal to $\Delta y = 0.00375h$ at $y = \pm h/2$ and to $\Delta y = 0.03h$ for $2.5h \leqslant y \leqslant 8h$. Finally, a number of 219 points are used in the spanwise direction, giving a mesh spacing $\Delta z = 0.015h$. The maximum mesh spacing of $0.03h$ allows acoustic waves to be well calculated up to the Strouhal number $St = fh/u_j = 5.6$, where f is the frequency. Note, moreover, that in the physical domain the grids are stretched at rates lower than 1 % in order to preserve numerical accuracy.

3. Aerodynamic results

3.1. *Flow snapshots*

Three-dimensional isosurfaces of density are represented in figure 2 for JetL3.9 and JetL9.1 in order to visualize the shear layers of the jets. Both small- and very large-
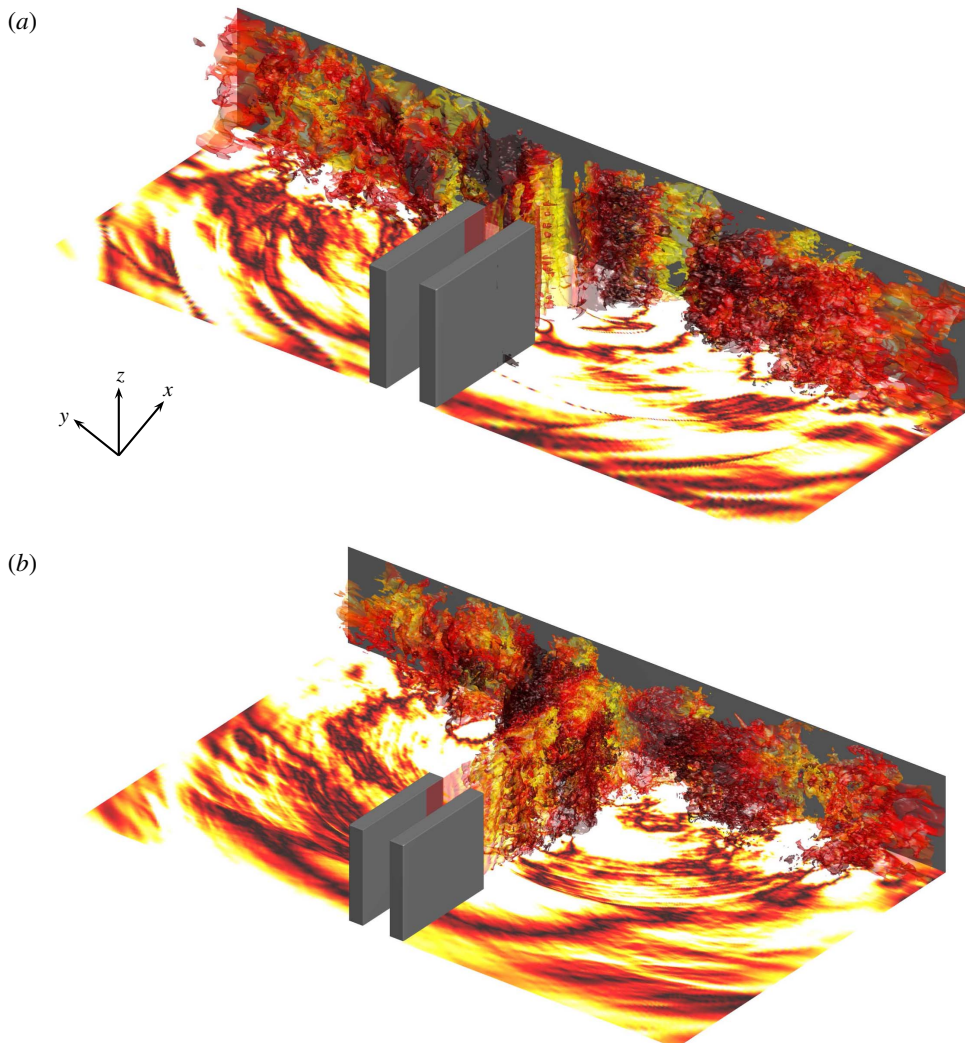
(*a*)

(*b*)

FIGURE 2. (Colour online) Representation for (*a*) JetL3.9 and (*b*) JetL9.1 of the isosurfaces of density associated with 1.25 kg m^{-3}, coloured by the local Mach number, and of the pressure fluctuations in the plane (x, y) using a colour scale ranging from -7500 to 7500 Pa, from white to red. The nozzle and the flat plate are in grey.

scale structures are visible. The near acoustic fields obtained in the plane (x, y) are also shown. For the two jets, acoustic waves appear clearly to come from the region of jet impact.

Snapshots of the vorticity norm obtained in the plane (x, y) and in the plane (x, z) at $y = -h/2$, are represented in figure 3. For JetL3.9, the two shear layers exhibit in the (x, y) plane large-scale structures, of typical size $0.5h$, which do not seem to be organized symmetrically with respect to the jet axis. In the spanwise direction, large- and small-scale structures, namely vorticity tubes along the entire spanwise extent and structures of typical size $0.05h$, can both be seen. Besides, the spanwise correlation of the flow structures appears significant near the nozzle but also near the flat plate.
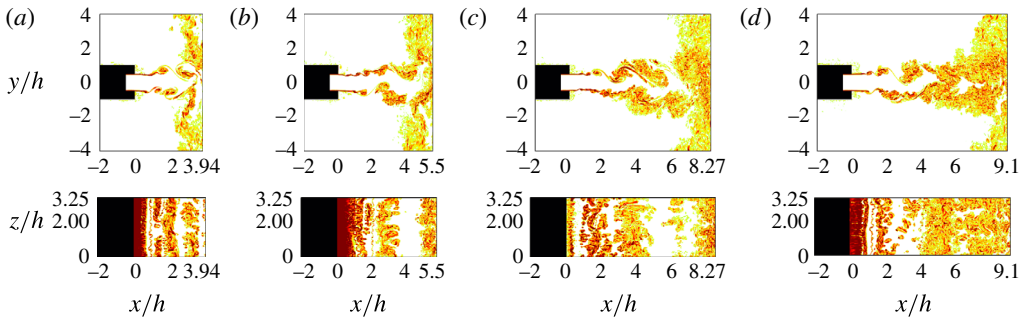
FIGURE 3. (Colour online) Snapshots in the plane (x, y) and in the plane (x, z) at $y = -h/2$ of the vorticity norm $|\omega|$ for (a) JetL3.9, (b) JetL5.5, (c) JetL8.3 and (d) JetL9.1. The colour scale ranges up to the level of $10u_j/h$, from white to red. The nozzle is in black.

For JetL5.5, JetL8.3 and JetL9.1, large-scale structures are still visible in the shear layers, but their spanwise correlations is relatively weak far from the nozzle. Overall, however, a nearly two-dimensional organization of the vortical structures is visible in the shear layers, as observed experimentally for supersonic rectangular impinging jets by Krothapalli (1985) and Norum (1991) and by Thurow *et al.* (2002) using real-time flow visualization techniques.

Density and fluctuating pressure fields obtained in the (x, y) plane for the four jets are provided in figure 4 and movie 1 available at https://doi.org/10.1017/jfm.2016.628. In all cases, large-scale structures and sound waves are observed in the shear layers and outside the jet, respectively. For JetL3.9 and JetL5.5, the pressure waves come from the region of jet impact, and are organized antisymmetrically with respect to the jet axis. For JetL8.3 and JetL9.1, two acoustic components appear in the pressure fields. The first components consist of circular waves centred around $x \simeq 2h$ in the jet shear layers. The second components propagate from the region of jet impact, mostly in the upstream direction. They are similar but weaker than those observed for JetL3.9 and JetL5.5.

3.2. *Mean flow fields*

Mean velocity fields obtained in the (x, y) plane are shown in figure 5. As expected, very small variations, of only approximately 4 % of the jet exit velocity, are noted near the axis, indicating that the jets are almost ideally expanded. In all cases, a stagnation point is visible on the flat plate at $y = 0$, and two plane wall jets are created after the jet impact. Important parameters of wall jets include the maximum velocity u_{max}, the distance x_{max} from the wall at which the velocity reaches u_{max} and the distance $x_{1/2}$ at which the velocity has dropped to $u_{max}/2$, refer to Irwin (1973) and George *et al.* (2000) for instance. The values calculated at $y = 2h$ for the present wall jets are given in table 2. For a greater nozzle-to-plate distance, the wall jet maximum velocity is found to be lower, as expected. In parallel, the wall jet thickness x_{max} is smaller, whereas the wall jet thickness $x_{1/2}$ is larger.

3.3. *Velocity fluctuations*

The peak root-mean-square values of axial and transverse velocity fluctuations u' and v' calculated in the present jets between the nozzle lip and the flat plate are shown in
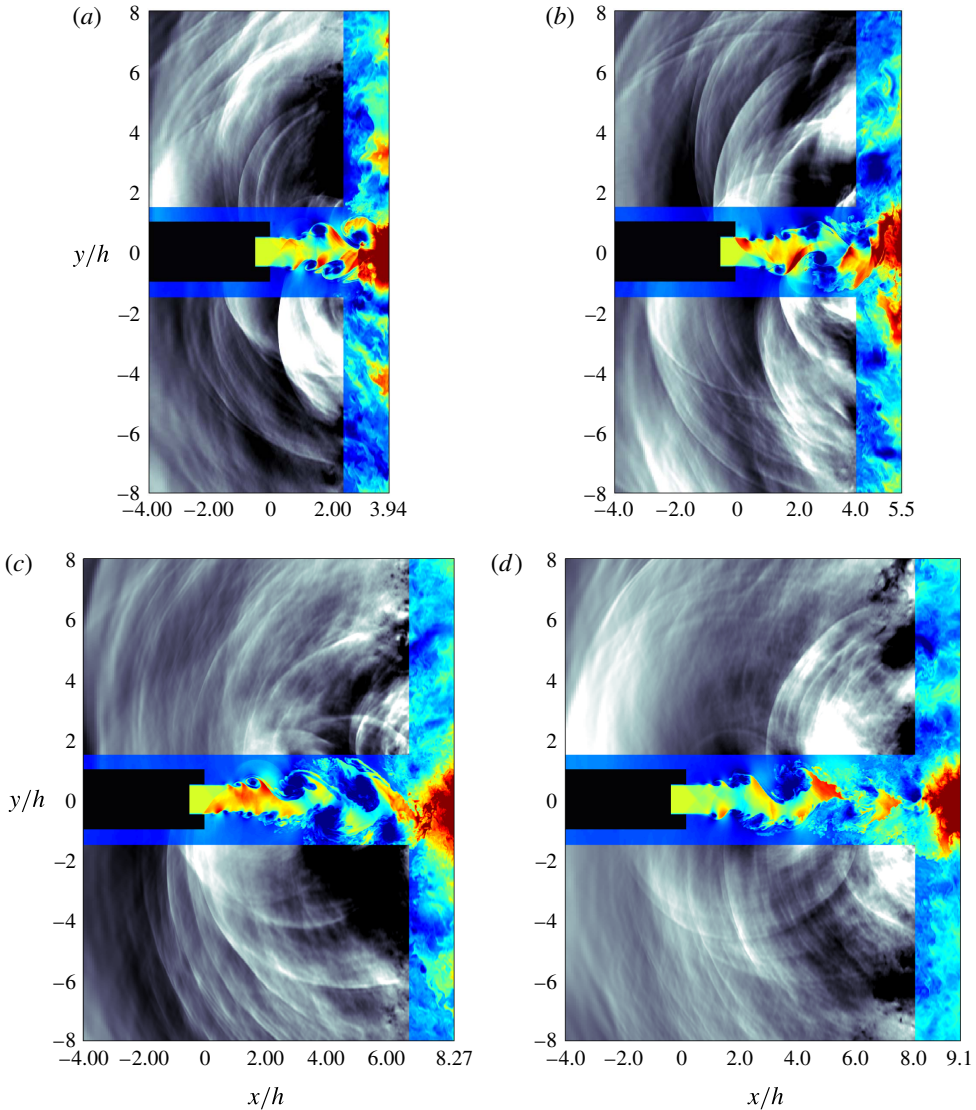
FIGURE 4. (Colour online) Snapshots in the (x, y) plane of the density in the jet and close to the flat plate and of the pressure fluctuations for (a) JetL3.9, (b) JetL5.5, (c) JetL8.3 and (d) JetL9.1. The colour scale ranges from 1 to 2 kg m^{-3} for density, from blue to red and from -7500 to 7500 Pa for pressure, from black to white. The nozzle is in black.

figures 6(a) and 6(b), respectively. For JetL3.9 and JetL5.5, the maximal root-mean-square values for the axial velocity are found around $x = 0.5h$, and are equal to 31.8 % and 32.7 % of the jet exit velocity u_j, respectively. For JetL8.3 and JetL9.1, they are located farther downstream, around $x = 0.75h$, and reach 26.6 % and 27.3 % of u_j. In all cases, other peak values are observed just upstream of the flat plate. They decrease with the nozzle-to-plate distance, yielding 28.5 %, 27.3 %, 24.4 % and 24 % of u_j for JetL3.9, JetL5.5, JetL8.3 and JetL9.1. For the transverse velocity, higher root-mean-square values are obtained for JetL3.9 and JetL5.5 than for JetL8.3 and JetL9.1. In
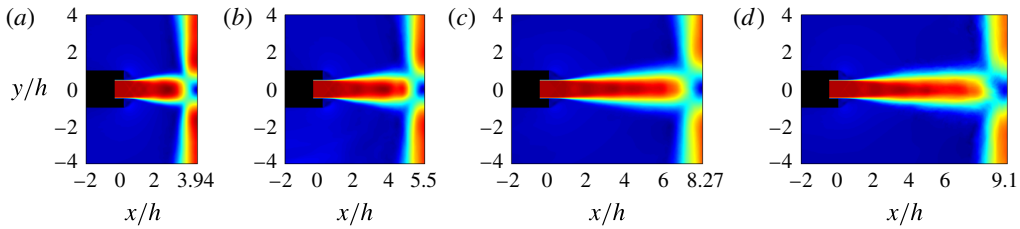
FIGURE 5. (Colour online) Mean velocity field obtained in the (x, y) plane for (a) JetL3.9, (b) JetL5.5, (c) JetL8.3 and (d) JetL9.1. The colour scale ranges from 0 to 400 m s^{-1}, from blue to red. The nozzle is in black.
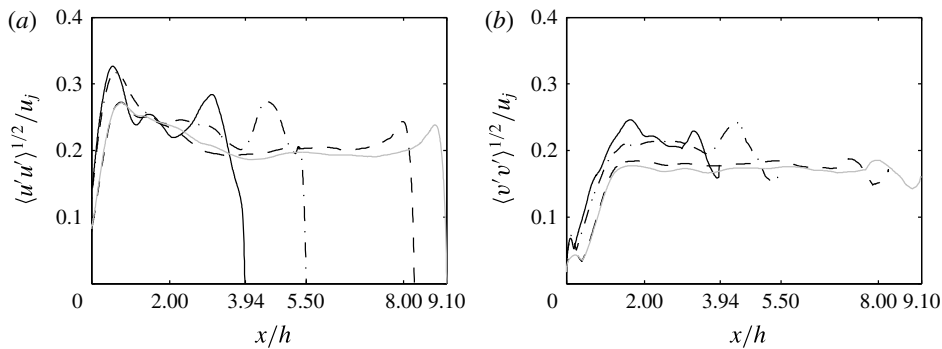

FIGURE 6. Axial variations of the peak root-mean-square values of velocity fluctuations (a) u' and (b) v' for —— JetL3.9, — · — JetL5.5, – – – JetL8.3 and —— JetL9.1.

	u_{max} (m s^{-1})	x_{max}/h	$x_{1/2}/h$
JetL3.9	361	0.065	0.75
JetL5.5	349	0.051	0.83
JetL8.3	317	0.040	0.98
JetL9.1	300	0.039	1.00

TABLE 2. Maximum velocity u_{max}, thicknesses x_{max}/h and $x_{1/2}/h$ of the wall jets at $y = 2h$.

particular, the maximal values, obtained at $x \simeq 1.7h$ in all cases, are approximately 21 % of the jet exit velocity for JetL3.9 and JetL5.5 and 17.5 % for JetL8.3 and JetL9.1.

3.4. *Convection velocity*

The evolution of the shear-layer turbulent structures and more precisely their convection velocity are important features to understand the aeroacoustic feedback mechanism. For two pressure-matched parallel streams with equal specific heats, Papamoschou & Roshko (1988) defined for instance the convection Mach number $\mathcal{M}_c$ as

$$\mathcal{M}_c = \frac{u_1 - u_2}{a_1 + a_2} = \frac{u_1 - u_c}{a_1} = \frac{u_c - u_2}{a_2}, \tag{3.1}$$
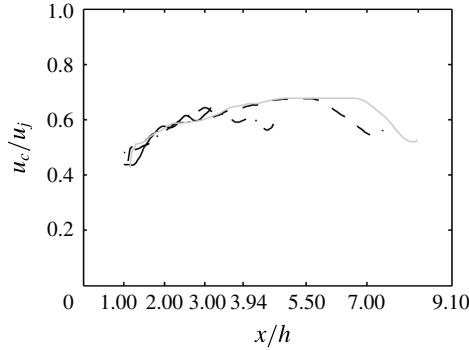
FIGURE 7. Convection velocity of the turbulent structures in the shear layers for ——— JetL3.9, — · — JetL5.5, – – – JetL8.3 and ——— JetL9.1.

where u_1 and u_2 are the velocities and a_1 and a_2 are the speeds of sound in the high-speed and low-speed streams, and u_c is the theoretical isentropic convection velocity. For the present jets, one gets $u_1 = u_j$ and $u_2 = 0$ and $a_1 = a_j = \sqrt{\gamma R T_j}$ and $a_2 = a_0 = \sqrt{\gamma R T_0}$, where T_j and T_0 are the temperatures in the jet and in the ambient medium and $R = 287$ J kg^{-1} K^{-1} is the specific gas constant. The convection velocity is thus given by

$$u_c = \frac{u_j}{a_j/a_0 + 1} \tag{3.2}$$

providing $u_c = 0.57 u_j$ for the present jets.

In this study, the local convection velocity at axial position x along the lipline at $y = -h/2$ is computed from cross-correlations of axial velocity fluctuations between two points located at $x \pm 0.1h$. The results obtained are shown in figure 7. In the four jets, the convection velocity is close to $0.50 u_j$ at $x = h$, increases farther downstream, reaches a peak around $x = 2h$ and then decreases. The peak values are equal to $0.62 u_j$, $0.64 u_j$, $0.67 u_j$ and $0.68 u_j$ for JetL3.9, JetL5.5, JetL8.3 and JetL9.1, respectively. Overall, the mean convection velocity along the lipline is around $0.60 u_j$. This value is in good agreement with the theoretical value of $0.57 u_j$, and with the value of $0.60 u_j$ measured by Panda, Raman & Zaman (1997) for an ideally expanded rectangular jet at a Mach number of $\mathcal{M}_j = 1.3$.

4. Acoustic results

4.1. *Sound pressure levels*

The sound pressure levels obtained at $x = 0$ and $y = 1.5h$ are displayed in figure 8 as a function of the Strouhal number $St = fh/u_j$. Several tones are found to emerge, especially for JetL3.9 and JetL5.5, as observed experimentally by Norum (1991) for a supersonic rectangular impinging jet. The frequencies of the tones, whose levels are at least 5 dB higher than the broadband noise level, are given in table 3.

For JetL3.9, in figure 8(*a*), seven tones appear. As obtained by Tam & Norum (1992) for cold rectangular supersonic jets, their frequencies are the linear combinations of two tone frequencies, at Strouhal numbers $St_1 = 0.115$ and $St_2 = 0.255$, yielding $St_3 = St_1 + St_2$, $St_4 = 2St_1 + St_2$, $St_5 = St_1 + 2St_2$, $St_6 = 2St_1 + 2St_2$ and $St_7 = 3St_1 + 2St_2$. These seven tone frequencies were also found in the experiments of Thurow *et al.* (2002) for a jet corresponding to that considered in the LES. Eight
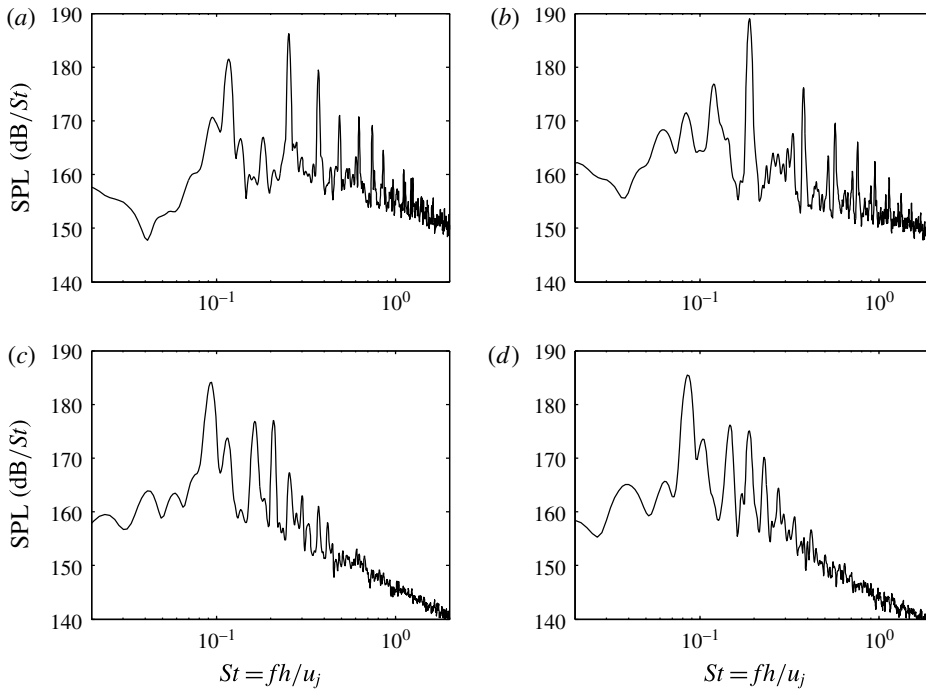
FIGURE 8. Sound pressure levels (SPL) at $x = 0$ and $y = 1.5h$ as a function of the Strouhal number St for (*a*) JetL3.9, (*b*) JetL5.5, (*c*) JetL8.3 and (*d*) JetL9.1.

	St_1	St_2	St_3	S_4	St_5	St_6	St_7
JetL3.9	0.115	**0.255**	0.37	0.485	0.625	0.74	0.855
JetL5.5	0.12	**0.19**	0.38	0.57	0.76	0.95	1.14
JetL8.3	**0.092**	0.165	0.21	0.255	—	—	—
JetL9.1	**0.085**	0.145	0.19	0.23	—	—	—

TABLE 3. Strouhal numbers emerging in the spectra of figure 8. The Strouhal numbers of the dominant tones are in bold.

other tone frequencies were measured, most likely due to the rectangular geometry of the nozzle, allowing additional oscillation modes along the transverse direction. For JetL5.5, in figure 8(*b*), a fundamental tone at $St_2 = 0.19$ and its first six harmonics are seen. This result is in good agreement with the experiments of Thurow *et al.* (2002), in which a fundamental tone at $St = 0.20$ was acquired. Another tone at $St_1 = 0.12$ is also visible in the present spectrum. For JetL8.3 and JetL9.1, in figure 8(*c,d*), four tones appear, the fourth tone is at a Strouhal number $St_4 = St_1 + St_2$. Only the third ones, at $St_3 = 0.21$ and $St_3 = 0.19$, respectively, are observed experimentally by Thurow *et al.* (2002). In these cases where the nozzle-to-plate distances are equal to $8.27h$ and $9.1h$, significant differences can however be expected between the LES and the experiments given the aspect ratio of 3 of the rectangular nozzle in the experiments. Note finally that the strongest resonance is obtained for JetL5.5 for which a maximum sound pressure level of 188 dB/St is reached. This was also the case in the experiments.
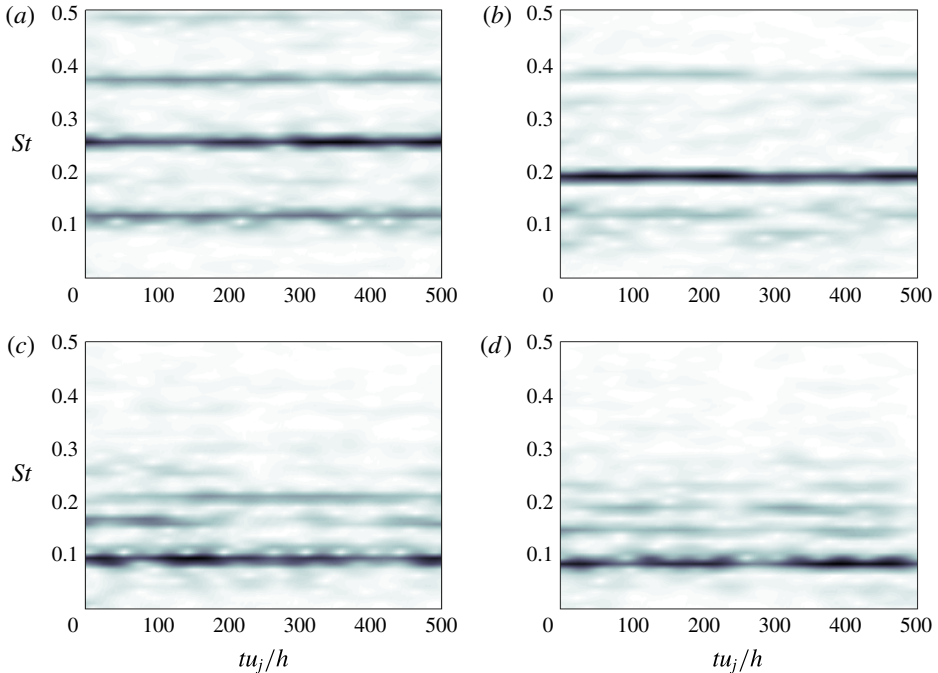
FIGURE 9. Spectra of the pressure fluctuations computed using a sliding window at $x = 0$ and $y = 1.5h$ as functions of time and Strouhal number for (*a*) JetL3.9, (*b*) JetL5.5, (*c*) JetL8.3 and (*d*) JetL9.1.

In order to determine whether the different tones are produced alternatively or simultaneously in the jets, a Fourier transform is applied to the pressure fluctuations at $x = 0$ and $y = 1.5h$ using a sliding window of size $35u_j/h$. The spectra thus calculated are represented in figure 9 as functions of time and Strouhal number. For JetL3.9, the three main tones at $St_1 = 0.115$, $St_2 = 0.255$ and $St_3 = 0.37$ obtained above are clearly visible, and seem to coexist. For JetL5.5, the dominant tone at $St_2 = 0.19$, the tone at $St_1 = 0.12$ and their harmonic at $St_3 = 0.38$ appear at the same time. Finally, for JetL8.3 and JetL9.1, the dominant tones at $St_1 = 0.092$ and $St_1 = 0.085$, respectively, and the tones at St_2, St_3 and St_4 can be seen. The amplitudes of the tones at St_2, St_3 and St_4 seem to vary in time. Moreover, given the results reported in §5 about the nature of the jet oscillations at the tone frequencies, the coexistence of the tones in most cases suggests that the jets undergo symmetric and antisymmetric oscillations at the same time. This is in good agreement with the experimental observations made by Tam & Norum (1992) for a supersonic rectangular impinging jet using a stroboscopic light source.

4.2. *Tone frequencies*

In order to explain the origin of the tones generated by impinging jets, Powell (1953) proposed a mechanism consisting of two steps. First, in the jet shear layers, a coherent structure is convected downstream from the nozzle to the plate. It impinges on the plate, and then generates an acoustic wave propagating upstream. This wave is reflected back by the nozzle lip, which excites the shear layer, and leads to the formation of a new coherent structure. The period T_0 of this feedback loop is given
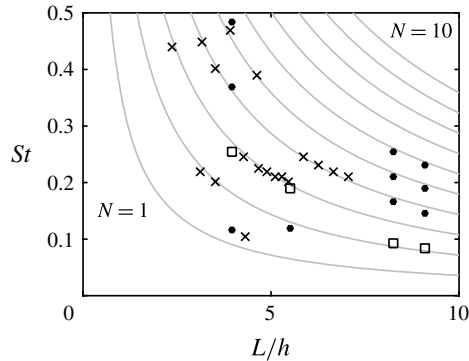
FIGURE 10. Representation of the Strouhal numbers of the □ dominant and ● secondary tones in the present jets as a function of the nozzle-to-plate distance L/h; × experimental data of Thurow *et al.* (2002). The grey lines show the Strouhal numbers predicted by (4.2) using $\langle u_c \rangle = 0.60 u_j$.

by the sum of the time necessary for a shear-layer structure to travel from the nozzle down to the plate and of the time of propagation of an acoustic wave from the plate up to the nozzle, yielding

$$T_0 = \int_0^L \frac{1}{u_c(x)} \, \mathrm{d}x + \frac{L}{a_0} = \frac{N+p}{f}, \tag{4.1}$$

where $u_c(x)$ is the local convection velocity in the shear layers, a_0 is the speed of sound in the ambient medium, p is a phase lag and the mode number N indicates the number of times the feedback mechanism occurs during the period T_0. According to Powell (1953), the phase lag p is not necessarily null because the reflection of the acoustic wave on the nozzle lip and the creation of a coherent structure in the shear layers do not happen simultaneously. Nevertheless, by setting $p = 0$, Ho & Nosseir (1981) and Nosseir & Ho (1982) proposed the following model in order to predict the frequencies of the feedback mechanism, writing

$$\frac{L}{\langle u_c \rangle} + \frac{L}{a_0} = \frac{N}{f}, \tag{4.2}$$

where $\langle u_c \rangle$ is the mean convection velocity of the turbulent structures in the shear layers between the nozzle and the plate.

The Strouhal numbers of the tones reported in table 3 for the present jets are represented in figure 10 as a function of the nozzle-to-plate distance. Only the fundamental tone frequencies, which are not harmonics of other tone frequencies and which will be called source tone frequencies in the following, are shown. The tone frequencies obtained in the experiments of Thurow *et al.* (2002), and those given by relation (4.2) using a mean convection velocity of $0.60 u_j$ are also plotted.

The tone Strouhal numbers in the LES are found to be in agreement with the experimental results, but also to be well predicted by the model equation. The source tones are associated with the first, third, fourth and fifth modes of the model for JetL3.9, with the second and third modes for JetL5.5 and with the second, fourth, fifth and sixth modes for JetL8.3 and JetL9.1. Moreover, the dominant tones in JetL3.9 and

	JetL3.9	JetL5.5	JetL8.3	JetL9.1
SPL (dB/St)	185	188	182	183
Skewness factor	0.39	0.57	0.27	0.29
Kurtosis factor	3.16	3.87	3.36	3.25

TABLE 4. Maximal levels in the sound spectra of figure 8, at $x = 0$ and $y = 1.5h$, and skewness and kurtosis factors of the fluctuating pressure at $x = 0$ and $y = 8.5h$.

JetL5.5 and those in JetL8.3 and JetL9.1 appear to be connected, respectively, with the third and second modes of the model. A similar staging behaviour of the dominant tone frequency as the nozzle-to-plate distance increases was observed experimentally by Krothapalli (1985) for a rectangular supersonic impinging jet.

4.3. *Skewness and kurtosis factors*

The nonlinear effects on the propagation of the acoustic waves generated by the jets are investigated by looking at the statistical properties of the pressure fluctuations at $x = 0$ and $y = 8.5h$, at a distance far from the region of jet impingement in order to eventually obtain steep wave fronts. The skewness and the kurtosis factors calculated for the four jets are reported in table 4. Positive values of skewness between 0.27 and 0.57 are found. They appear to be higher when the peak level in the pressure spectra at $x = 0$ and $y = 1.5h$, also provided in the table, increases. In particular, the strongest skewness and kurtosis values are reached for JetL5.5, which is also the most resonant case with a maximum sound level of 188 dB/St at $x = 0$ and $y = 1.5h$.

For JetL5.5, in which the strongest resonance is obtained as mentioned above, the time variations of the pressure fluctuations recorded at $x = 0$ and $y = 8.5h$ are represented in figure 11(*a*) over the entire simulation time for $0 \leqslant t \leqslant 500h/u_j$, and in figure 11(*b*) for $230h/u_j \leqslant t \leqslant 270h/u_j$. The probability density function of the full pressure signal is also shown in figure 11(*c*). Weak shock waves and N-shaped waves with sharp compressions associated with gradual expansions are visible in figure 11(*b*). Similar observations were made by Baars & Tinney (2013, 2014) in the acoustic field of a jet at Mach 3 and by de Cacqueray & Bogey (2014) for an overexpanded jet at $\mathcal{M}_j = 3.3$. In addition, at certain times, the pressure fluctuations exceed 15 % of the ambient pressure. This is notably the case at $t = 242h/u_j$ and $t = 253h/u_j$, where two strong shock waves are found. Finally, the skewness factor is equal to 0.57, and thus exceeds the value of 0.4 which indicates the probable presence of crackle noise according to Ffowcs-Williams, Simson & Virchis (1975).

5. Analysis of the aeroacoustic feedback mechanism

5.1. *Fourier decomposition of the pressure field*

In order to determine the amplitude and phase fields associated with the different tones of the feedback loop in the four jets, a Fourier transform in time is applied to the near pressure fields recorded every 50th LES time step in the (x, y) plane. The results obtained for the dominant tone frequencies are represented in figure 12.

The phase fields in the bottom views of figure 12 allow us to identify the nature of the oscillation modes associated with the tones. For JetL3.9 and JetL5.5, these modes are antisymmetric given the 180° phase shift visible with respect to the jet axis in figure 12(*e*,*f*). For JetL8.3 and JetL9.1, on the contrary, they are symmetric since
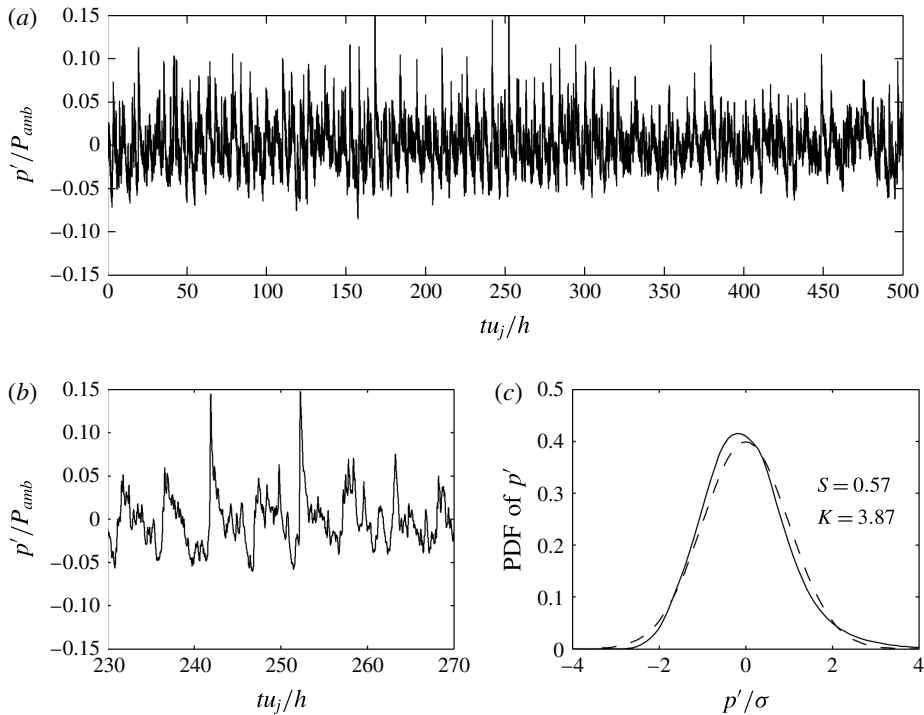
FIGURE 11. Pressure fluctuations at $x = 0$ and $y = 8.5h$ for JetL5.5: (*a*) time variations over the entire simulation, (*b*) variations over a short period and (*c*) —— probability density function and – – – probability density function of a Gaussian distribution where σ represents the standard deviation of p'.

the phase is identical on both sides of the jet axis in figure 12(*g*,*h*). Symmetric and antisymmetric oscillation modes were also found experimentally by Norum (1991) at the tone frequencies of rectangular supersonic impinging jets.

The amplitude fields in the top views of figure 12 all exhibit a cell structure between the nozzle and the plate. By considering the two semi-cells near the nozzle and the plate as one cell, the cell structure appears to contain three cells for JetL3.9 and JetL5.5 in figure 12(*a*,*b*) and two cells for JetL8.3 and JetL9.1 in figure 12(*c*,*d*). Thus, at the dominant tone frequency, the number of cells is equal the mode number predicted by the model of Ho & Nosseir (1981), namely three for the two first jets and two for the others. Besides, it can be noted that the amplitude levels near the jet axis in figure 12(*a*,*b*) are very weak, as expected for antisymmetric oscillations.

The amplitude fields of figure 12 also provide information on the sound sources at the dominant tone frequencies. For JetL3.9, three acoustic components labelled (i), (ii) and (iii) are revealed by the spots of intense levels in figure 12(*a*). The first component can be seen on both sides of the jet for $0 < \alpha < 20°$, where α is the angle between the upstream direction and the propagation direction from the impingement region as illustrated in the figure. It is related to the upstream-propagating neutral acoustic waves of the jet, which will be further discussed later. The second acoustic component is visible for $30 < \alpha < 50°$. It seems to propagate from a point around $x = 2.5h$ and $y = 1.5h$, where strong pressure levels are found. Finally, the third acoustic component is noted for $\alpha > 60°$. It may be generated near the flat plate
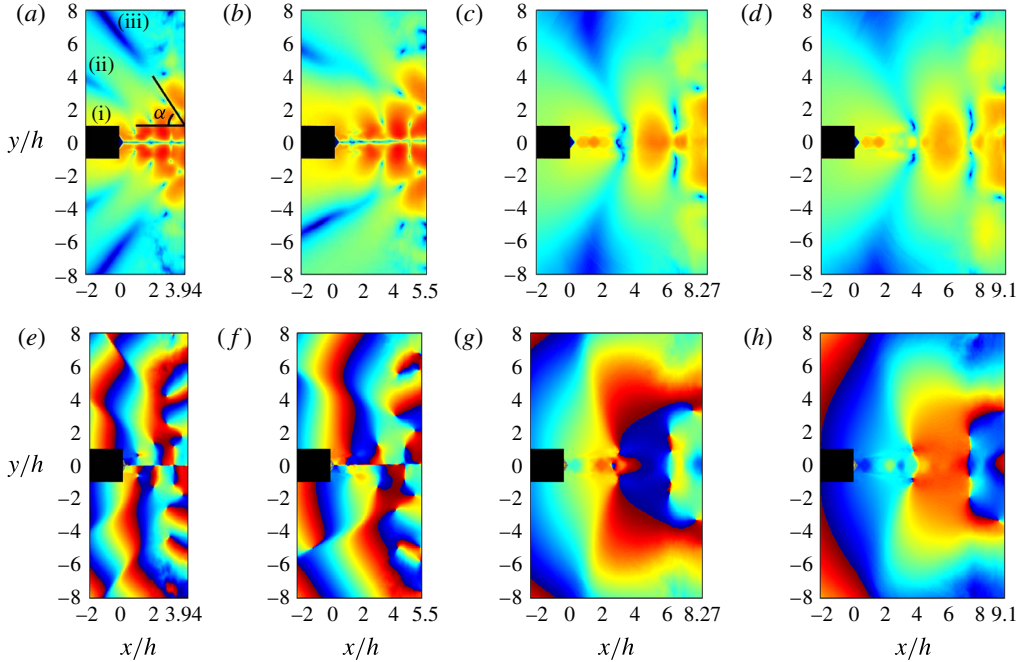
FIGURE 12. (Colour online) Amplitude (*a*–*d*) and phase (*e*–*h*) fields obtained for the dominant tones in (*a,e*) JetL3.9 at $St = 0.255$, (*b,f*) JetL5.5 at $St = 0.19$, (*c,g*) JetL8.3 at $St = 0.092$ and (*d,h*) JetL9.1 at $St = 0.085$.

around $y = 3h$ where, again, high pressure levels are obtained. For JetL5.5, two acoustic components can be observed in figure 12(*b*), for $0 < \alpha < 30°$ and for $\alpha > 40°$. As for JetL3.9, the first one may be due to the upstream-propagating neutral acoustic waves of the jet, and the second one may be produced near the plate around $y = 3.5h$. Finally, for JetL8.3 and JetL9.1, two acoustic contributions appear to similarly emerge.

5.2. *Model of an hydrodynamic–acoustic standing wave*

In self-sustaining oscillating flows, hydrodynamic–acoustic standing waves can be observed, as was the case in the screeching free supersonic jets of Panda *et al.* (1997) and Panda & Seasholtz (1999). These waves are due to the superposition of hydrodynamic waves propagating downstream and acoustic waves propagating upstream.

A simple model can be built to determine the wavenumber of the hydrodynamic–acoustic standing waves in the present jets. By denoting ω the angular frequency of the feedback mechanism, and k_p and k_a the wavenumbers of the hydrodynamic and acoustic waves, the fluctuating pressure in the jet shear layers can be written as

$$p'(x, t) = A_a \sin(k_a x + \omega t + \phi_a) + A_p \sin(k_p x - \omega t + \phi_p), \qquad (5.1)$$

where A_a, A_p and ϕ_a and ϕ_p are the amplitudes and phase shifts of the acoustic and hydrodynamic waves. The quadratic mean value is then equal to

$$p'_{rms}(x) = \frac{1}{T} \int_0^T p'(x, t)^2 \, dt = \frac{A_a^2}{2} + \frac{A_p^2}{2} - A_a A_p \cos((k_a + k_p)x + \phi_a + \phi_p), \qquad (5.2)$$

where $T = 2\pi/\omega$ is the time period. Therefore, at the frequency of the feedback mechanism, the pattern of a standing wave with a wavenumber

$$k_{sw} = k_p + k_a \tag{5.3}$$

is expected. By considering that $k_{sw} = 2\pi/L_{sw}$, $k_p = \omega/u_c$ and $k_a = \omega/a_0$, where L_{sw} is the wavelength of the hydrodynamic–acoustic standing wave, u_c is the convection velocity in the jet shear layers and a_0 is the ambient speed of sound, one gets

$$\frac{1}{L_{sw}} = \frac{f}{a_0} + \frac{f}{u_c}, \tag{5.4}$$

where $f = 2\pi/\omega$. In the amplitude fields of figure 12, there is a whole number N of cells between the nozzle lip and the flat plate. Assuming that the cell structures result from the presence of hydrodynamic–acoustic standing waves, this indicates that the nozzle-to-plate distance is a multiple of the wavelength L_{sw}, that is $L = NL_{sw}$, yielding

$$\frac{N}{f} = \frac{L}{a_0} + \frac{L}{u_c}. \tag{5.5}$$

This equation is identical to (4.2) given by the model of Ho & Nosseir (1981), demonstrating that the number of cells in the standing wave is also the mode number. This result is consistent with the observations made in the previous section. The aeroacoustic feedback loop establishing between the nozzle and the plate thus leads to the formation of hydrodynamic–acoustic standing waves.

5.3. *Wave analysis using a vortex sheet model of the jet*

In the analytical study of small-amplitude waves in jets of Tam & Hu (1989), three families of instability waves were identified: the Kelvin–Helmholtz instability waves, which correspond to vorticity waves, and the supersonic and subsonic instability waves, which are acoustic waves (Berman & Williams 1970; Mack 1990; Sabatini & Bailly 2014). On the basis of this result, Tam & Norum (1992) suggested that the acoustic waves of the feedback loop in impinging jets are linked to the acoustic subsonic instability waves of the jets. These waves are found to be unstable for jets with mixing layers of finite thickness. For jets with mixing layers modelled by a vortex sheet (Tam & Hu 1989), on the contrary, they are neutral, and have a real angular frequency, but also a real wavenumber.

In this work, as previously done by Tam & Norum (1992) for planar jets and Tam & Ahuja (1990) for round jets, a wave analysis is therefore carried out using a vortex sheet model in order to better describe the feedback loop in impinging jets. More precisely, the neutral acoustic waves of an ideally expanded 2-D jet of height h, exit velocity u_j and Mach number $\mathcal{M}_j$, bounded by two vortex sheets, are investigated. A schematic representation of a symmetric instability of such a jet is provided in figure 13.

The pressure fluctuations, associated with small-amplitude disturbances superimposed on the mean flow inside and outside of the jet are denoted by p_{int} and p_{ext}, and the lateral displacement of the upper vortex sheet is given by $\zeta(x, t)$. The linearized continuity, momentum and energy equations for a compressible inviscid fluid

$$\left. \begin{aligned} \Delta p_{ext} - \frac{1}{a_0^2}\frac{\partial^2 p_{ext}}{\partial t^2} &= 0 \quad \text{outside the jet,} \\ \Delta p_{int} - \frac{1}{a_j^2}\left(\frac{\partial^2 p_{int}}{\partial t^2} + u_j^2\frac{\partial^2 p_{int}}{\partial x^2}\right) &= 0 \quad \text{inside the jet,} \end{aligned} \right\} \tag{5.6}$$
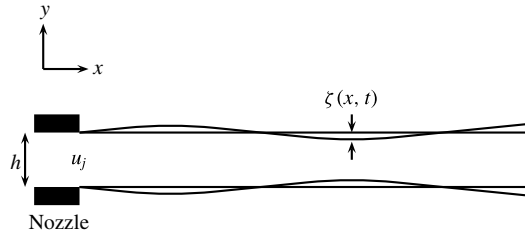
FIGURE 13. Symmetric instability of a 2-D supersonic jet bounded by vortex sheets.

where a_0 and a_j are the sound speeds in the ambient medium and in the jet, are considered. The boundary conditions on the upper vortex sheet located at $y = h/2$ are

$$\left.\begin{aligned}
p_{int} &= p_{ext}, \\
\frac{\partial^2 \zeta}{\partial t^2} &= -\frac{1}{\rho_0}\frac{\partial p_{ext}}{\partial y}, \\
\frac{\partial^2 \zeta}{\partial t^2} + u_j^2 \frac{\partial^2 \zeta}{\partial x^2} &= -\frac{1}{\rho_j}\frac{\partial p_{int}}{\partial y},
\end{aligned}\right\} \tag{5.7}$$

where ρ_0 are the densities in the ambient medium and in the jet. On the centreline, the boundary conditions for symmetric and antisymmetric modes are different, yielding

$$\left.\begin{aligned}
\frac{\partial p_{int}}{\partial y} &= 0 \quad \text{for symmetric modes,} \\
p_{int} &= 0 \quad \text{for antisymmetric modes.}
\end{aligned}\right\} \tag{5.8}$$

The equation system (5.6) being closed, wave solutions of the form

$$\begin{bmatrix} p_{int}(x,y,t) \\ p_{ext}(x,y,t) \\ \zeta(x,t) \end{bmatrix} = \begin{bmatrix} \hat{p_{int}}(y) \\ \hat{p_{ext}}(y) \\ \hat{\zeta} \end{bmatrix} e^{i(kx-\omega t)}, \tag{5.9}$$

where k and ω are the wavenumber and the angular frequency of the wave, can be sought. Two dispersion relations were found by Tam & Norum (1992). They are given by

$$\frac{[(\omega - u_j k)^2/a_j^2 - k^2]^{1/2}\rho_0\omega^2}{(k^2 - \omega^2/a_0^2)^{1/2}\rho_j(\omega - u_j k)^2} + \tan\left\{\left[\frac{(\omega - u_j k)^2}{a_j^2} - k^2\right]^{1/2}h/2\right\} = 0 \tag{5.10}$$

for symmetric modes, and

$$\frac{[(\omega - u_j k)^2/a_j^2 - k^2]^{1/2}\rho_0\omega^2}{(k^2 - \omega^2/a_0^2)^{1/2}\rho_j(\omega - u_j k)^2} + 1/\tan\left\{\left[\frac{(\omega - u_j k)^2}{a_j^2} - k^2\right]^{1/2}h/2\right\} = 0 \tag{5.11}$$

for antisymmetric modes.

The solutions of the dispersion relations (5.10) and (5.11) calculated for the present jet are represented in figure 14 as functions of the Strouhal number and the wavenumber. Three symmetric neutral acoustic wave modes, referred to as S1, S2
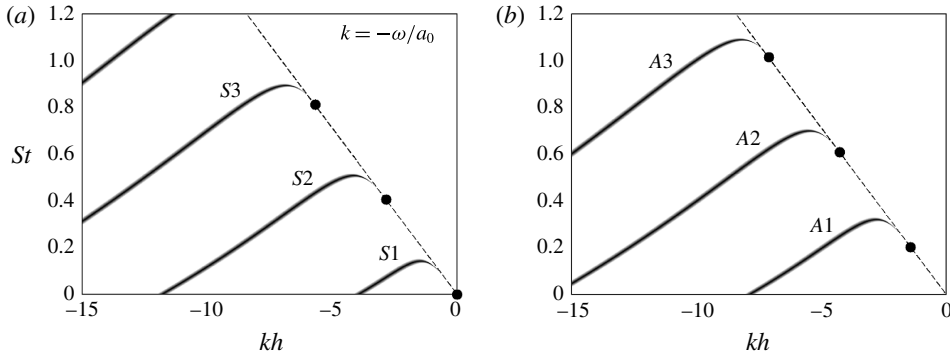
FIGURE 14. Dispersion relations for (*a*) the symmetric and (*b*) the antisymmetric neutral acoustic wave modes for an ideally expanded planar jet with $\mathcal{M}_j = 1.28$, ● lower limits of the modes, $---$ $k = -\omega/a_0$.

and $S3$, appear in figure 14(*a*). In the same way, three antisymmetric modes denoted by $A1$, $A2$ and $A3$ are found in figure 14(*b*).

According to Tam & Hu (1989), upstream-propagating acoustic waves are present in high-speed jets. They are confined in the jets when the jets are subsonic, but lie outside when the jets are supersonic. Such waves are found in figure 14 on the right-hand side of each mode where $\mathrm{d}\,St/\mathrm{d}k < 0$, leading to a negative group velocity $\mathrm{d}\omega/\mathrm{d}k$. Allowable frequency ranges can thus be determined for the different modes. Their upper limits, which correspond to the maximum Strouhal numbers reached for the modes when $\mathrm{d}\,St/\mathrm{d}k = 0$, are obtained from the figure. Their lower limits are calculated, since they are necessarily associated with acoustic waves propagating with a group velocity of $-a_0$, and located on the dashed line of figure 14 defined by

$$k = -\frac{\omega}{a_0}. \tag{5.12}$$

For $k = -\omega/a_0$, the first terms in (5.10) and (5.11), and consequently the second terms, tend to infinity. The argument of the tangent function needs to be equal to

$$\left[\frac{(\omega - u_j k)^2}{a_j^2} - k^2\right]^{1/2} \frac{h}{2} = \frac{n - 1}{\pi} \tag{5.13}$$

for (5.10) and

$$\left[\frac{(\omega - u_j k)^2}{a_j^2} - k^2\right]^{1/2} \frac{h}{2} = \frac{n - 1/2}{\pi} \tag{5.14}$$

for (5.11), yielding the following Strouhal numbers for the lower limits of the allowable frequency ranges

$$St = \frac{n - 1}{u_j((1 + u_j/a_0)^2/a_j^2 - 1/a_0^2)^{1/2}} \tag{5.15}$$

for the symmetric modes and

$$St = \frac{n - 1/2}{u_j((1 + u_j/a_0)^2/a_j^2 - 1/a_0^2)^{1/2}} \tag{5.16}$$

for the antisymmetric modes, where n is the mode number. The values calculated for the present jet are depicted in figure 14.
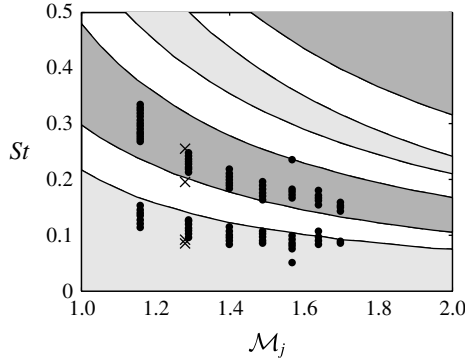
FIGURE 15. Allowable frequency ranges for the upstream-propagating neutral acoustic wave modes as a function of the exit Mach number; symmetric modes are in light grey and antisymmetric modes are in dark grey; ● dominant tone frequencies in the experiments of Tam & Norum (1992) for rectangular supersonic cold jets and × dominant tone frequencies in the present LES.

The allowable frequency ranges determined for the two first symmetric and antisymmetric upstream-propagating wave modes are represented in figure 15 as a function of the exit Mach number $\mathcal{M}_j$. The dominant tone frequencies measured by Tam & Norum (1992) for cold rectangular impinging jets at Mach numbers between 1.15 and 1.70, for a large number of nozzle-to-plate distances in each case, are also shown. Two modes, namely a low-frequency symmetric mode and a high-frequency antisymmetric mode are observed in most cases. The dominant tone frequencies obtained for the four jets at $\mathcal{M}_j = 1.28$ in the LES are also plotted in the figure. The tone frequencies for JetL3.9 and JetL5.5, at $St_2 = 0.255$ and $St_2 = 0.19$, respectively, fall into the allowable range for the first symmetric mode, whereas the tone frequencies for JetL8.3 and JetL9.1, at $St_1 = 0.092$ and $St_1 = 0.085$, lie in the allowable range for the first antisymmetric mode. Considering the results in § 5.2, the present wave analysis thus appears to predict the nature of the jet oscillation mode at the dominant tone frequencies, which is symmetric for the two first jets but antisymmetric for the two others. However, it only provides allowable frequency ranges. In order to better understand how, for a given nozzle-to-plate distance, discrete frequencies are selected over these ranges, this analysis is combined below with the aeroacoustic feedback model.

5.4. Combination of the aeroacoustic feedback model and the wave analysis

The aeroacoustic feedback model and the wave analysis based on the vortex sheet model are combined in order to determine both the most likely possible tone frequencies of the feedback mechanism and the antisymmetric or symmetric nature of the corresponding modes. This is made possible by assuming that the acoustic wavenumber in the feedback loop is equal to the opposite of the wavenumber k of the upstream propagating acoustic waves found in the wave analysis. Thus, the (5.3) relating the wavenumber k_{sw} of the hydrodynamic–acoustic standing wave due to the feedback mechanism and the acoustic and hydrodynamic wavenumbers k_a and k_p leads to

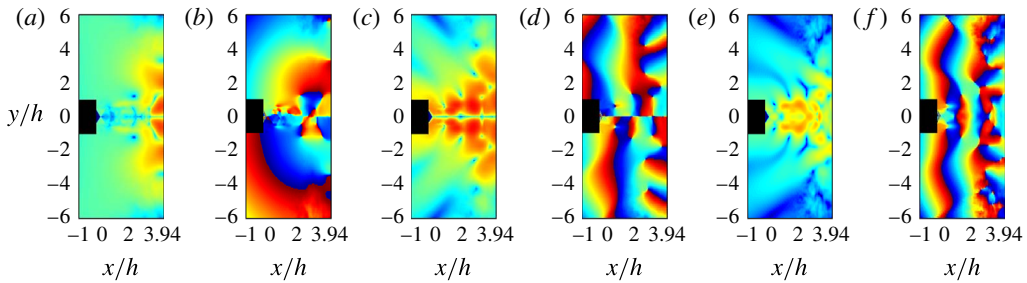$$f = \frac{Nu_c}{L} + k\frac{u_c}{2\pi} \tag{5.17}$$

FIGURE 16. (Colour online) Amplitude (*a,c,e*) and phase (*b,d,f*) fields obtained for the three dominant tones of JetL3.9 at $St_1 = 0.115$, $St_2 = 0.255$ and $St_3 = 0.37$, from left to right.

given that $k_{sw} = 2\pi N/L$, $k_p = 2\pi f/u_c$ and $k_a = -k$. The feedback model and the wave analysis are then combined by representing this relation and the dispersion relations in the same figure for the different impinging jets. The results will be compared with the simulation results.

For JetL3.9, the phase and the amplitude fields obtained by LES for the three main tones at $St_1 = 0.115$, $St_2 = 0.255$ and $St_3 = 0.37$ are displayed in figure 16. For $St_1 = 0.115$, a 180° phase shift with respect to the jet axis is found in the phase field of figure 16(*b*), indicating an antisymmetric oscillation mode. No cell structure clearly appears in the amplitude field of figure 16(*a*), suggesting the absence of an hydrodynamic–acoustic standing wave in this case. For $St_2 = 0.255$, an antisymmetric oscillation mode is observed in figure 16(*d*), and a cell structure containing three cells between the nozzle and the plate is visible in figure 16(*d*). Finally, for $St_3 = 0.37$, a symmetric oscillation mode and a cell structure with four cells are revealed by figure 16(*e,f*).

The results obtained for JetL3.9 by combining the feedback model and the wave analysis are represented in figure 17 by showing the dispersion relations of the acoustic wave modes for a planar jet at $\mathcal{M}_j = 1.28$ together with the solutions of (5.17) for the first ten modes of the feedback mechanism, as functions of the Strouhal number and the wavenumber. The three dominant tones are also indicated on the line $k = -\omega/a_0$, depending on the symmetric or antisymmetric nature of the corresponding oscillation modes. In figure 17(*a*), the tone at $St_3 = 0.37$ is found just below the symmetric mode $S2$ of the jet, on the line associated with the mode $N = 4$ of the feedback loop. This is consistent with the results reported above for $St_3 = 0.37$. In figure 17(*b*), the tone at $St_2 = 0.255$ is located at the intersection of the antisymmetric mode $A1$ of the jet and of the mode $N = 3$ of the feedback loop. Again, this result is in agreement with the phase and amplitude fields provided by the LES. Finally, the tone at $St_1 = 0.115$ does not seem to be predicted by the model combination. It is not surprising given that St_1 is equal to $St_3 - St_2$, and that there is no hydrodynamic–acoustic standing wave in figure 16(*a*).

The phase and the amplitude fields obtained for JetL5.5 at the two main tone frequencies at $St_1 = 0.12$ and $St_2 = 0.19$ are displayed in figure 18. The phase fields indicate a symmetric oscillation mode for the first tone and an antisymmetric oscillation mode for the second one. Moreover, cell structures containing two and three cells, respectively, between the nozzle and the plate appear in the amplitude fields.
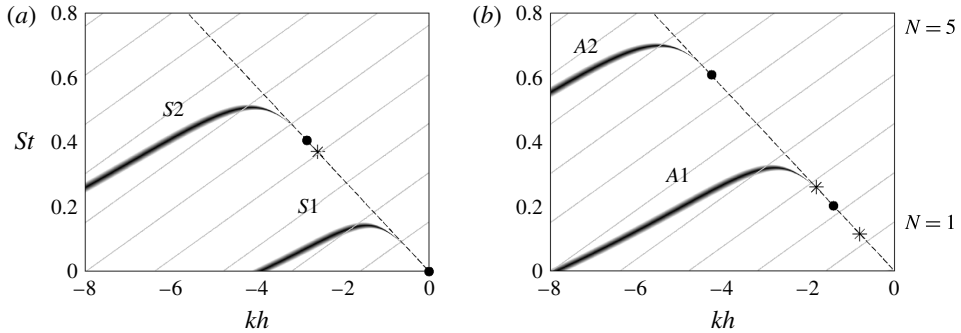
FIGURE 17. Representation of —— the dispersion relations for (*a*) the symmetric and (*b*) the antisymmetric neutral acoustic wave modes for an ideally expanded planar jet with $\mathcal{M}_j = 1.28$, ● lower limits of the modes, – – – $k = -\omega/a_0$, —— relation (5.17) for $L = 3.94h$, ∗ dominant tone frequencies of JetL3.9.
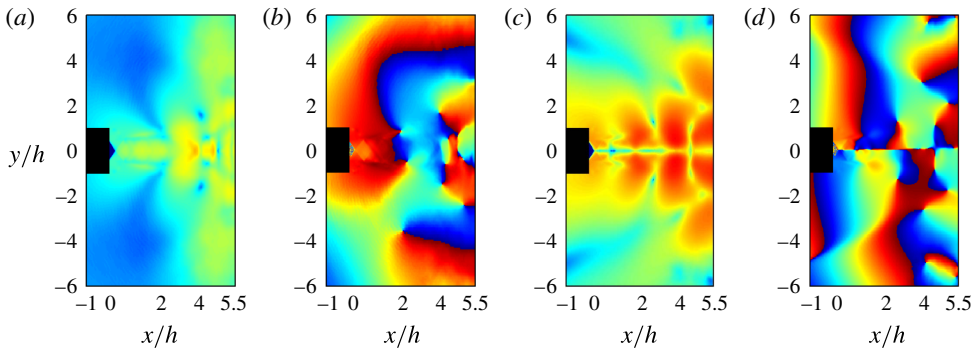

FIGURE 18. (Colour online) Amplitude (*a,c*) and phase (*b,d*) fields obtained for the two dominant tones of JetL5.5 at $St_1 = 0.12$ and $St_2 = 0.19$, from left to right.

The results of the model combination for JetL5.5 are shown in figure 19, in which the two dominant tones obtained in the LES for this jet are also represented. In figure 19(*a*), the tone at $St_1 = 0.12$ lies at the intersection of the symmetric mode $S1$ of the jet and of the second mode of the feedback loop, which is in agreement with the tone properties observed in figure 18(*a,b*). In figure 19(*b*), the tone at $St_2 = 0.19$ is located very near the antisymmetric mode $A1$ of the jet and on the third mode of the feedback loop, which is also in line with the amplitude and phase fields of figure 18(*c,d*).

The phase and amplitude fields obtained for JetL8.3 at the four main tone frequencies, at $St_1 = 0.092$, $St_2 = 0.165$, $St_3 = 0.21$ and $St_4 = 0.255$ are given in figure 20. For the first tone, a symmetric oscillation mode and a cell structure containing two cells are seen in figure 20(*a,b*). For the three other tones, antisymmetric oscillation modes and cell structures containing four, five and six cells, respectively, are noted in figure 20(*c–h*).

The results of the model combination for JetL8.3 and the four dominant tones in this jet are displayed in figure 19. In figure 21(*a*), the first tone at $St_1 = 0.092$ is very close to the intersection of the symmetric jet mode $S1$ and the second mode of the feedback loop. In figure 21(*b*), the second, third and fourth tones are found near or
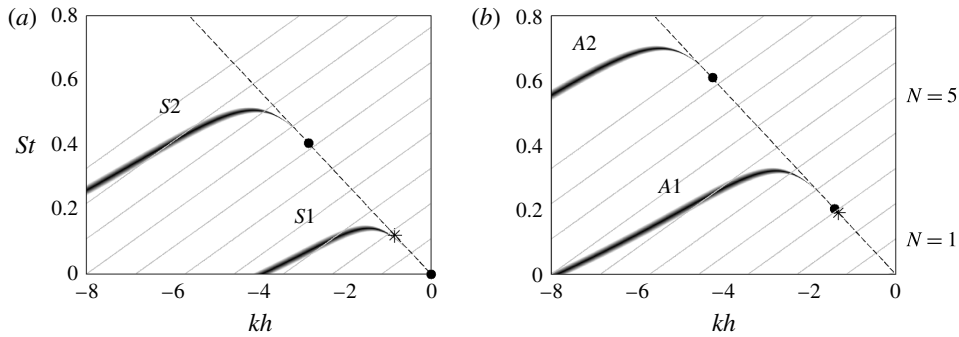
FIGURE 19. Representation of —— the dispersion relations for (*a*) the symmetric and (*b*) the antisymmetric neutral acoustic wave modes for an ideally expanded planar jet with $\mathcal{M}_j = 1.28$, ● lower limits of the modes, $---\ k = -\omega/a_0$, —— relation (5.17) for $L = 5.5h$, ∗ dominant tone frequencies of JetL5.5.
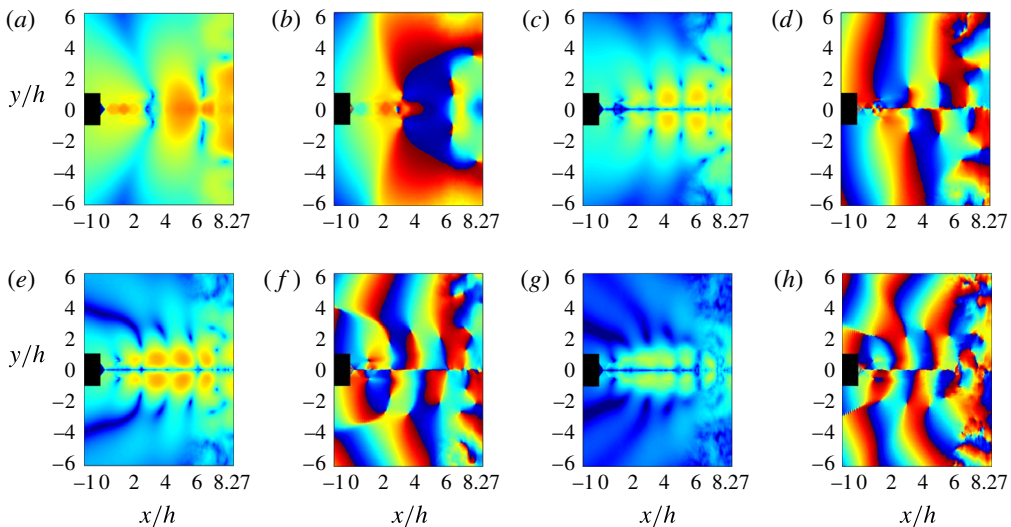

FIGURE 20. (Colour online) Amplitude (*a,c,e,g*) and phase (*b,d,f,h*) fields obtained for the four dominant tones of JetL8.3 (*a–d*) at $St_1 = 0.092$ and $St_2 = 0.165$, and (*e–h*) at $St_3 = 0.21$ and $St_4 = 0.255$, from left to right.

on the antisymmetric mode *A*1 of the jet and on the fourth, fifth and sixth modes of the feedback loop, respectively. These findings are consistent with the amplitude and phase fields of figure 20.

For brevity, the amplitude and phase fields obtained for JetL9.1 at the four main tone frequencies and the results given by the model combination in this case are not presented, because they are very similar to those reported above for JetL8.3.

In summary, the proposed model combination applies successfully to the present impinging jets. The tone frequencies obtained in the LES lie near the lower limits of the allowable ranges predicted by the wave analysis for the upstream-propagating acoustic wave modes. This trend can be due to the fact that, in the vicinity of the lower limits of the modes, the group velocity of the neutral acoustic waves is very
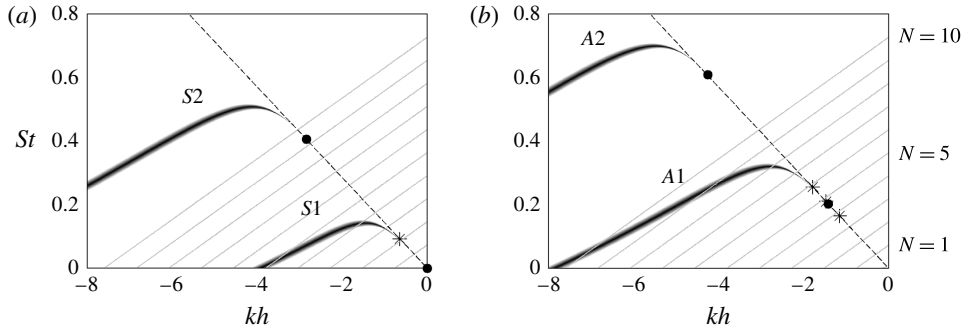
FIGURE 21. Representation of —— the dispersion relations for (*a*) the symmetric and (*b*) the antisymmetric neutral acoustic wave modes for an ideally expanded planar jet with $\mathcal{M}_j = 1.28$, ● lower limits of the modes, $---$ $k = -\omega/a_0$, —— relation (5.17) for $L = 8.27h$, $*$ dominant tone frequencies of JetL8.3.

close to $-a_0$. Consequently, these waves are the most likely to sustain an acoustic feedback. Having noted this, it seems possible to predict the most probable tones, their frequencies and their symmetric or antisymmetric natures. For the antisymmetric modes, the tone frequencies can be expected to be located near the lower limit of the mode $A1$, as is the case for the four jets of this study. For the symmetric modes, they can be found near the lower limit of the mode $S2$, as for JetL3.9, but also at the intersections between the modes $S1$ and the different modes of the feedback loop, as for the other jets. Obtaining a tone frequency at the first intersection point between the mode $S1$ and the mode $N = 1$ of the feedback loop is however unlikely given the very low Strouhal number $St < 0.05$ at this point.

Finally, note that a similar wave analysis can be performed for jets with mixing layers of finite thickness, as in Tam & Ahuja (1990). In this case, the frequencies of the lower limits of the allowable bands for the upstream-propagating acoustic wave modes are lower than using the vortex sheet model. This could explain why tone frequencies are found just below the lower limits of allowable bands for JetL3.9, JetL8.3 and JetL9.1 in the present study.

6. Conclusion

In this paper, the flow and the near pressure fields of an ideally expanded planar jet at a Mach number of 1.28 and a Reynolds number of 5×10^4 impinging on a flat plate at four distances from the nozzle between 3.94 and 9.1 nozzle heights have been presented. Overall, the numerical results obtained by large-eddy simulation using low-dissipation schemes compare well with experimental data and with theoretical models available in the literature. This is the case, in particular, for the mean convection velocity of the turbulent structures in the shear layers, and for the frequencies of the several dominant tones emitted by the jets. These tones are shown to be generated, as expected, by aeroacoustic feedback loops establishing between the nozzle lips and the flat plate, which result in the presence of hydrodynamic–acoustic standing waves in the jets. The frequencies of these tones are therefore well predicted by the classical aeroacoustic feedback model.

In order to better determine which tone frequencies are likely to be emerge among those given by the aeroacoustic feedback model, and whether a symmetric or an

antisymmetric jet oscillation will be found at each of these frequencies, a wave analysis has been conducted for a planar jet with mixing layers modelled by a vortex sheet. It provides allowable bands for the upstream-propagating acoustic waves, which are assumed to close the aeroacoustic feedback loops. The tone frequencies obtained in the LES fall in these bands. More importantly, by combining the wave analysis and the aeroacoustic feedback model, it has been demonstrated that it is possible to predict the most probable tones, their frequencies, and the symmetric or antisymmetric natures of the corresponding jet oscillations.

Acknowledgements

Supplementary movie

Supplementary movie is available at https://doi.org/10.1017/jfm.2016.628.

REFERENCES

ARTHURS, D. & ZIADA, S. 2012 Self-excited oscillations of a high-speed impinging planar jet. *J. Fluids Struct.* **34**, 236–258.

BAARS, W. J. & TINNEY, C. E. 2013 Quantifying crackle-inducing acoustic shock-structures emitted by a fully-expanded mach 3 jet. *AIAA Paper* 2013-2081.

BAARS, W. J. & TINNEY, C. E. 2014 Shock-structures in the acoustic field of a mach 3 jet with crackle. *J. Sound Vib.* **333** (12), 2539–2553.

BERLAND, J., BOGEY, C. & BAILLY, C. 2007a Numerical study of screech generation in a planar supersonic jet. *Phys. Fluids* **19**, 075105.

BERLAND, J., BOGEY, C., MARSDEN, O. & BAILLY, C. 2007b High-order, low dispersive and low dissipative explicit schemes for multiple-scale and boundary problems. *J. Comput. Phys.* **224** (2), 637–662.

BERMAN, C. H. & WILLIAMS, J. E. 1970 Instability of a two-dimensional compressible jet. *J. Fluid Mech.* **42** (1), 151–159.

BOGEY, C. & BAILLY, C. 2004 A family of low dispersive and low dissipative explicit schemes for flow and noise computations. *J. Comput. Phys.* **194** (1), 194–214.

BOGEY, C. & BAILLY, C. 2006 Large eddy simulations of transitional round jets: influence of the Reynolds number on flow development and energy dissipation. *Phys. Fluids* **18**, 065101.

BOGEY, C. & BAILLY, C. 2009 Turbulence and energy budget in a self-preserving round jet: direct evaluation using large eddy simulation. *J. Fluid Mech.* **627**, 129–160.

BOGEY, C., DE CACQUERAY, N. & BAILLY, C. 2009 A shock-capturing methodology based on adaptative spatial filtering for high-order non-linear computations. *J. Comput. Phys.* **228** (5), 1447–1465.

BOGEY, C. & MARSDEN, O. 2016 Simulations of initially highly disturbed jets with experiment-like exit boundary layers. *AIAA J.* **54** (2), 1299–2016.

BOGEY, C., MARSDEN, O. & BAILLY, C. 2011 Large-eddy simulation of the flow and acoustic fields of a Reynolds number 10^5 subsonic jet with tripped exit boundary layers. *Phys. Fluids* **23**, 035104.

BOGEY, C., MARSDEN, O. & BAILLY, C. 2012 Influence of initial turbulence level on the flow and sound fields of a subsonic jet at a diameter-based Reynolds number of 10^5. *J. Fluid Mech.* **701**, 352–385.

BUCHMANN, N. A., MITCHELL, D. M., INGVORSEN, K. M., HONNERY, D. R. & SORIA, J. 2011 High spatial resolution imaging of a supersonic underexpanded jet impinging on a flat plate. In *6th Australian Conference on Laser Diagnostics in Fluid Mechanics and Combustion, Canberra, Australia, 5–7 December 2011*.

DE CACQUERAY, N. & BOGEY, C. 2014 Noise of an overexpanded mach 3.3 jet: non-linear propagation effects and correlations with flow. *Intl J. Aeroacoust.* **13** (7), 607–632.

DE CACQUERAY, N., BOGEY, C. & BAILLY, C. 2011 Investigation of a high-mach-number overexpanded jet using large-eddy simulation. *AIAA J.* **49** (10), 2171–2182.

FAUCONNIER, D., BOGEY, C. & DICK, E. 2013 On the performance of relaxation filtering for large-eddy simulation. *J. Turbul.* **14** (1), 22–49.

FFOWCS-WILLIAMS, J. E., SIMSON, J. & VIRCHIS, V. J. 1975 Crackle: an annoying component of jet noise. *J. Fluid Mech.* **71** (02), 251–271.

GEORGE, W. K., ABRAHAMSSON, H., ERIKSSON, J., KARLSSON, R. I., LÖFDAHL, L. & WOSNIK, M. 2000 A similarity theory for the turbulent plane wall jet without external stream. *J. Fluid Mech.* **425**, 367–411.

HENDERSON, B., BRIDGES, J. & WERNET, M. 2005 An experimental study of the oscillatory flow structure of tone-producing supersonic impinging jets. *J. Fluid Mech.* **542**, 115–137.

HENDERSON, B. & POWELL, A. 1993 Experiments concerning tones produced by an axisymmetric choked jet impinging on flat plates. *J. Sound Vib.* **168** (2), 307–326.

HO, C. M. & NOSSEIR, N. S. 1981 Dynamics of an impinging jet. Part 1. The feedback phenomenon. *J. Fluid Mech.* **105**, 119–142.

HOURIGAN, K., RUDMAN, M. & BROCHER, E. 1996 The feedback loop in impinging two-dimensional high-subsonic and supersonic jets. *Exp. Therm. Fluid Sci.* **12** (2), 265–270.

IRWIN, H. P. A. H. 1973 Measurements in a self-preserving plane wall jet in a positive pressure gradient. *J. Fluid Mech.* **61** (1), 33–63.

KREMER, F. & BOGEY, C. 2015 Large-eddy simulation of turbulent channel flow using relaxation filtering: resolution requirement and Reynolds number effect. *Comput. Fluids* **17** (7), 17–28.

KROTHAPALLI, A. 1985 Discrete tones generated by an impinging underexpanded rectangular jet. *AIAA J.* **23** (12), 1910–1915.

KROTHAPALLI, A., RAJKUPERAN, E., ALVI, F. & LOURENCO, L. 1999 Flow field and noise characteristics of a supersonic impinging jet. *J. Fluid Mech.* **392**, 155–181.

MACK, L. M. 1990 On the inviscid acoustic-mode instability of supersonic shear flows. *Theor. Comput. Fluid Dyn.* **2** (2), 97–123.

MITCHELL, D. M., HONNERY, D. R. & SORIA, J. 2012 The visualization of the acoustic feedback loop in impinging underexpanded supersonic jet flows using ultra-high frame rate schlieren. *J. Vis.* **15** (4), 333–341.

NORUM, T. D. 1991 Supersonic rectangular jet impingement noise experiments. *AIAA J.* **29** (7), 1051–1057.

NOSSEIR, N. S. & HO, C. M. 1982 Dynamics of an impinging jet. Part 2. The noise generation. *J. Fluid Mech.* **116**, 379–391.

PANDA, J., RAMAN, G. & ZAMAN, K. B. M. Q. 1997 Underexpanded screeching jets from circular, rectangular and elliptic nozzles. *AIAA Paper* 97-1623.

PANDA, J. & SEASHOLTZ, R. G. 1999 Measurement of shock structure and shock-vortex interaction in underexpanded jets using rayleigh scattering. *Phys. Fluids* **11** (12), 3761–3777.

PAPAMOSCHOU, D. & ROSHKO, A. 1988 The compressible turbulent shear layer: an experimental study. *J. Fluid Mech.* **197**, 453–477.

POWELL, A. 1953 On edge tones and associated phenomena. *Acta Acust.* **3**, 233–243.

RISBORG, A. & SORIA, J. 2009 High-speed optical measurements of an underexpanded supersonic jet impinging on an inclined plate. In *28th International Congress on High-Speed Imaging and Photonics*, 7126 (F), International Society for Optics and Photonics.

ROCKWELL, D. & NAUDASCHER, E. 1978 Review-self-sustaining oscillations of flow past cavities. *Trans. ASME J. Fluids Engng* **100** (2), 152–165.

SABATINI, R. & BAILLY, C. 2014 Numerical algorithm for computing acoustic and vortical spatial instability waves. *AIAA J.* **53** (3), 692–702.

TAM, C. K. W. & AHUJA, K. K. 1990 Theoretical model of discrete tone generation by impinging jets. *J. Fluid Mech.* **214**, 67–87.

TAM, C. K. W. & DONG, Z. 1994 Wall boundary conditions for high-order finite-difference schemes in computational aeroacoustics. *Theor. Comput. Fluid Dyn.* **6**, 303–322.

TAM, C. K. W. & HU, F. Q. 1989 On the three families of instability waves of high-speed jets. *J. Fluid Mech.* **201**, 447–483.

TAM, C. K. W. & NORUM, T. D. 1992 Impingement tones of large aspect ratio supersonic rectangular jets. *AIAA J.* **30** (2), 304–311.

THUROW, B., SAMIMY, M. & LEMPERT, W. 2002 Structure of a supersonic impinging rectangular jet via real-time optical diagnostics. *AIAA Paper* 2002-2865.